

Uncovering Exceptional Contours in non-Hermitian Hyperbolic Matter

Nisarg Chadha¹ and Awadhesh Narayan^{2,*}

¹*Undergraduate Programme, Indian Institute of Science, Bangalore 560012, India*

²*Solid State and Structural Chemistry Unit,
Indian Institute of Science, Bangalore 560012, India*

(Dated: July 11, 2023)

Abstract

Hyperbolic lattices are starting to be explored in search of novel phases of matter. At the same time, non-Hermitian physics has come to the forefront in photonic, optical, phononic, and condensed matter systems. In this work, we introduce non-Hermitian hyperbolic matter and elucidate its exceptional properties in depth. We use hyperbolic Bloch theory to investigate band structures of hyperbolic lattices in the presence of non-Hermitian on-site gain and loss as well as non-reciprocal hopping. Using various analytical and numerical approaches we demonstrate widely accessible and tunable exceptional points and contours in $\{10,5\}$ tessellations, which we characterize using phase rigidity, energy scaling, and vorticity. We further demonstrate the occurrence of higher-order exceptional points and contours in the $\{8,4\}$ tessellations using the method of Newton polygons, supported by vorticity and phase rigidity computations. Finally, we investigate the open boundary spectra and densities of states to compare with results from band theory, along with a demonstration of boundary localisation. Our results unveil an abundance of exceptional degeneracies in hyperbolic non-Hermitian matter.

* awadhesh@iisc.ac.in

I. INTRODUCTION

Spaces with negative curvature emerge naturally in general relativity [1], and also find applications in graph theory [2], random walks [3], complexity theory [4], and quantum information theory [5]. The enhanced bulk connectivity of the system [6] makes hyperbolic surfaces an efficient candidate for data storage and communication, making these geometries ubiquitous in data science and electrical engineering. Recent works on networks of coupled microwave resonators and superconducting qubits [7, 8] provide more tangible insight into these ideas from the perspective of band theory.

The theoretical extension of ideas from band theory and topology to hyperbolic geometries [9] and their experimental realisations [7, 8] on tabletop experimental platforms have propelled hyperbolic lattices to the forefront in the search for novel phases of matter. Progress in physical realisations through circuit quantum electrodynamics has made hyperbolic lattices a readily available platform for exploring band theories on these models, therefore being a direct test of the influence of the geometry and the metric itself on the properties of the system. The deviation from the Euclidean metric due to negative curvature of hyperbolic surfaces endows interesting properties to the behaviour and interactions of the entities constrained to reside on them, such as the finite ratio of boundary sites to the total sites, the non-Abelian nature of the translation group, and the subsequent higher dimensional quotient group of the manifold in k -space.

The implications of the curvature of space on the dimensionality and the topology of the Brillouin zone have been recently studied in order to come up with a comprehensive picture of a hyperbolic band theory [9]. Very recent work on investigating the counterparts to well-known Euclidean models such as the Haldane, Kane-Mele [10] and the Qi-Wu-Zhang models [11] has catalogued and contrasted the behaviour of curved and flat spaces. The use of real-space invariants on flat projections of hyperbolic tessellations has shown topological phase transitions characteristic of Chern insulator phases accompanied by edge modes and a quantized conductance [11]. The topological phase has been shown to be robust to disorder, and topological Anderson insulator phase transitions are also shown through numerical computations of topological invariants in the presence of disorder. Furthermore, higher-order topological insulator phases have been discovered in hyperbolic tessellations in two dimensions [12, 13]. These phases show zero-dimensional corner edge states whose degeneracy

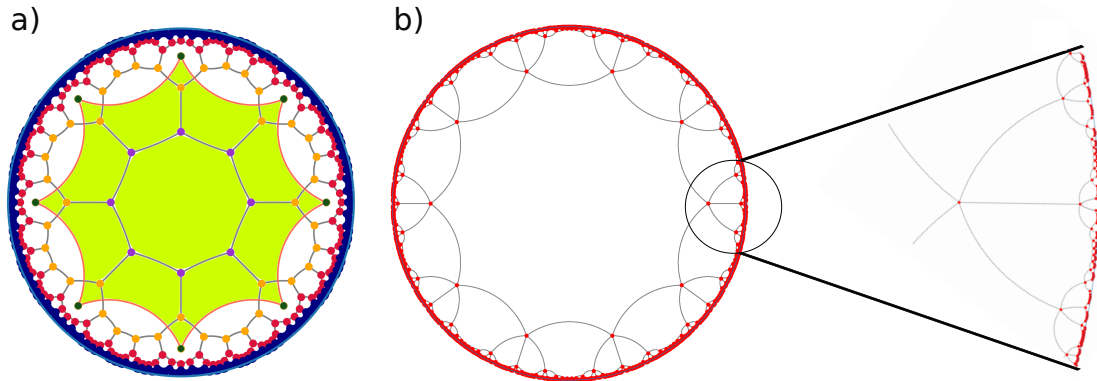


FIG. 1. **Visualising the hyperbolic plane in two dimensions through the Poincaré disk model.** (a) The $\{8,3\}$ tessellation with different coloured sites denoting different epochs generated recursively. The area in green shows the 16-site unit cell, also called the Bolza lattice, which itself is an $\{8,8\}$ tessellation. (b) The $\{10,5\}$ tessellation up to the first four epochs, along with a zoomed-in image showing the sites near the boundary.

depends on the symmetry of the crystal. The realisation of lattices with arbitrary rotational symmetries allows these corner edge states to have higher degeneracies than possible for Euclidean systems.

For real-space computation, the boundary sites play a much more prominent role in hyperbolic space than in flat space. Open boundary spectra show considerable deviations from the bulk spectra due to the macroscopic fraction of boundary sites, even in the thermodynamic limit. To circumvent this, Refs. 14 and 15 implemented a compactification of the hyperbolic manifold using regular maps to identify boundary sites and create a finite graph whilst removing the influence of dangling boundary sites. Remarkably, a universality in the shape of the Hofstadter butterfly is obtained when the unit cells in the compactified manifold are threaded by a flux [15]. These Hofstadter butterfly patterns are shown to be independent of the coordination number q for tessellations of the same p -gons.

In a parallel development, non-Hermitian systems have been in the limelight in recent years due to their intriguing fundamental properties, with a potential for interesting applications [16–20]. Beginning with the pioneering ideas of Bender and co-workers [21], the interplay with topology has reinvigorated the field and has led to several seminal discoveries. The role of topology in non-Hermitian systems is now at the forefront of research, with

implications for photonics, optics, metamaterials, topoelectric circuits and many others. Exceptional points are an important feature of non-Hermitian systems. These are singularities where eigenvalues and eigenvectors become identical [22–24], and have no counterpart in Hermitian systems. Not only are they interesting from a fundamental point of view – with remarkable associated properties such as Berry phases, Riemann sheet structures, and bulk Fermi arcs – they are also beginning to be exploited in applications. For instance, EPs have been used to design sensors with enhanced sensitivity [25–27]. Another intriguing phenomenon which has been recently identified in non-Hermitian systems is the non-Hermitian skin effect (NHSE), where a macroscopic fraction of states localize at the boundary [28–32]. NHSE is another topic of very active research in the past couple of years, whose implications are only beginning to be understood. It features intriguing connections to spectral topology and a plethora of experimental platforms have been used to implement its phenomenology [32, 33].

In this work, we explore the interplay of non-Hermiticity and hyperbolic geometry by using analytic band theory as well as numerical tight-binding calculations. We find that the higher order irreducible representations for the translational group lead to a greater degree of freedom in parameter space, which can allow tuning of parameters to readily obtain EPs as well as their higher dimensional analogues, exceptional contours. We investigate the behaviour of EPs in the presence of different kinds of non-Hermitian terms and characterise their properties. For ease of analytic computation, we use the $\{10,5\}$ tessellation due to its crystalline symmetry resulting in a two-site unit cell [34]. The $\{10,5\}$ tessellation lies in the same infinite crystalline family of $\{2(2g+1), 2g+1\}$ tessellations (with g being the genus) as the honeycomb lattice in Euclidean space, and has been termed "hyperbolic graphene" [34]. We introduce on-site gain and loss as well as non-reciprocal hopping to add non-Hermiticity and unveil the behaviour of the resulting exceptional contours using phase rigidity and vorticity to visualise the effects on the spectrum upon approaching such exceptional regions. The winding of eigenvalues near exceptional contours is calculated to display the inter-band vorticity intrinsic to the topology around an EP. Furthermore, we consider a model for an $\{8,4\}$ tessellation to show the occurrence of higher-order EPs upon introducing gain and loss in the system. We also utilize the recently proposed method of Newton polygons to obtain an analytic understanding of such higher-order EPs. Finally, we construct the real-space lattice using recursive circular inversions and use exact diagonalisation to obtain the energy

spectra and the densities of states. We compare the results obtained using the hyperbolic band theory and show deviations from exact diagonalisation. We also present boundary localisation effects in real space under non-reciprocal hopping. With greater freedom to tune parameters, along with current progress in circuit quantum electrodynamics and photonics, we hope our results can motivate creation of experimental platforms for realising sensors and other potential applications based on the synergy between hyperbolic connectivity and non-Hermiticity.

II. UNDERSTANDING HYPERBOLIC GEOMETRY

We briefly summarize here essential concepts in hyperbolic geometry as a foundation for the rest of our results. We will be interested in space-filling tilings of regular p -gons, with each vertex having a coordination number of q . This is denoted in the Schläfli notation as a $\{p,q\}$ tessellation. In this notation, the square lattice is a $\{4,4\}$ tessellation, and similarly, the honeycomb and triangular lattices are the $\{6,3\}$ and $\{3,6\}$ tessellations, respectively. Due to the restriction imposed by the angle sum property, these are the only permissible tessellations for Euclidean space. The absence of this restriction allows hyperbolic systems to have an infinite number of realisations of tessellations with higher p and q indices. These tessellations are projected onto flat space using the Poincaré disk model on a unit circle with distances measured in the Poincaré metric to obtain the lattices shown in Fig. 1 for the $\{8,3\}$ and $\{10,5\}$ tessellations.

For hyperbolic lattices, the lattice translation operators on the tessellation are elements of the discrete Fuchsian symmetry group [35], whose exact forms depend on the representation used for the lattice geometry. The discrete spatial symmetries of the tessellation allow the introduction of k -space momenta and automorphic Bloch wavefunctions for a hyperbolic band theory [9] in the same way as for Euclidean lattices. However, the elements of the Fuchsian group do not commute, and the non-Abelian nature of the Fuchsian group marks a striking deviation from Euclidean geometry. An automorphic band theory is expected to be incomplete for a hyperbolic lattice since the $U(1)$ phase attachment for automorphic wave functions forms a lower dimensional irreducible representation for the non-Abelian Fuchsian group. We shall subsequently visit the deviation between results from open boundary numerical diagonalisation and automorphic Bloch theory for different non-Hermitian param-

eters.

A. Generators of Translations in Hyperbolic Tessellations

Understanding the algebra of the translational operators is a crucial first step for a band theoretic description of hyperbolic lattices. For Euclidean geometries, the group of lattice translations forms a normal subgroup for the manifold whose quotient group gives the unit cell. Due to the commutative nature of the lattice translations, the d -dimensional Brillouin zone obtained is a \mathcal{S}^d surface with one-dimensional irreducible representations. As a result, using a $U(1)$ phase to describe systems with discrete translational symmetry gives the Bloch theorem, which describes the band structure for periodic systems in flat space.

On the other hand, for a hyperbolic surface, the quotient group of the hyperbolic manifold under the non-Abelian Fuchsian translational symmetry group gives a higher genus Riemann surface. This leads to a higher genus representation for the hyperbolic Brillouin zone, which is shown to be the Jacobian of the resulting Riemann surface [9]. This hyperbolic Brillouin zone has higher dimensional irreducible representations and cannot be described exactly by a $U(1)$ Bloch theorem.

The explicit form for the translation group operators $(\hat{\gamma}_1, \hat{\gamma}_2, \dots, \hat{\gamma}_n)$ is given in Ref. 8. We will use the same convention to attach the Bloch phase for inter-unit cell hoppings. According to the Bloch ansatz, a translation from a unit cell site i to a unit cell f carried out by subsequent applications of $\hat{\gamma}_{n_1}, \hat{\gamma}_{n_2}, \dots, \hat{\gamma}_{n_m}$ results in an addition of a $U(1)$ phase $\phi = \sum_{i=1}^m k_{n_i}$, where $k_{n_i} \in [0, 2\pi]$ is the phase associated with the application of $\hat{\gamma}_{n_i}$, with $n = 1, 2, \dots, m$. The number of independent group generators is determined by the exact structure (p and q) of the lattice. For the case of the $\{10,5\}$ tessellation, we have four independent generators $(\hat{\gamma}_1, \hat{\gamma}_2, \hat{\gamma}_3, \hat{\gamma}_4)$, resulting in a four-dimensional Brillouin zone with a genus of 2.

III. THE HYPERBOLIC TIGHT-BINDING MODEL

A. Description of the model in k -space

As elucidated in Ref. 34, the $\{10,5\}$ tessellation has a two-site unit cell and is part of the $\{2(2g+1), 2g+1\}$ infinite family of tessellations. We obtain two sublattices A and B,

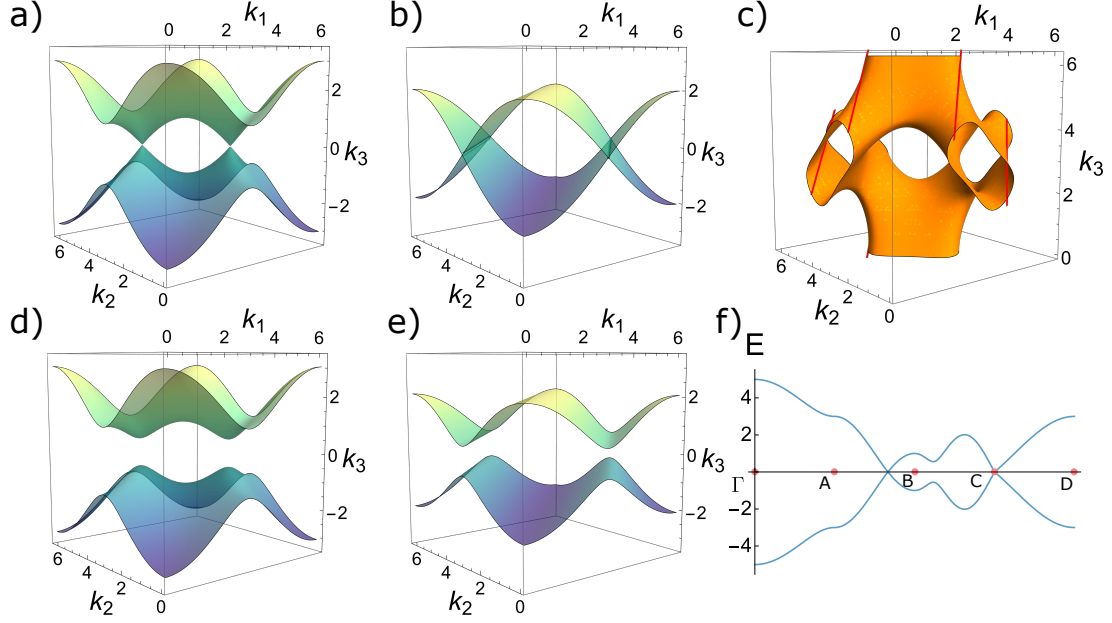


FIG. 2. **Visualising the energy spectra for Hermitian hyperbolic graphene.** (a) The energy spectrum with $M = 0$ produces the characteristic Dirac cones when $k_3 = 0$, $k_4 = \pi$ in which case $h(\mathbf{k}) = 1 + e^{ik_1} + e^{ik_2}$ becomes the phase factor for Euclidean graphene. (b) Nodal lines are obtained with $M = 0$ for $k_3 = 2\pi/3$ and $k_4 = 4\pi/3$, and the condition for band touching becomes $k_1 = k_2 \pm \pi$. Modulating k_3, k_4 gives different shapes of nodal surfaces. (c) The surface represents the allowed values of k_1, k_2, k_3 at which there is a k_4 that produces a node. The lines shown in red along the surface are the values of k_1, k_2, k_3 where $k_4 = 0$ gives a node. (d) Adding an on-site potential ($M \neq 0$) opens a gap in the system. For $k_3 = 0$, $k_4 = \pi$ a gapped spectrum ($\Delta E_g = 2M$) is obtained. The linear dispersion near the extrema is replaced by a quadratic dispersion ($|E| = \frac{(\Delta k)^2}{2M}$). (e) For $k_3 = 2\pi/3$, $k_4 = 4\pi/3$, a gapped system is obtained with the linear scaling being replaced by a quadratic scaling as in (d). (f) Energy spectrum through the Brillouin zone. The points defined here are $\Gamma(0,0,0,0)$, $A(\pi, 0, 0, 0)$, $B(\pi, 0, \pi, -\pi)$, $C(2\pi/3, -2\pi/3, 0, \pi)$, and $D(\pi, \pi, \pi, \pi)$.

similar to that for graphene, with each sublattice forming a $\{2g + 1, 2(2g + 1)\}$ tessellation of its own. To proceed with the hyperbolic Bloch ansatz in a tight binding model, we choose a unit cell and identify the nearest neighbours for the A sublattice in terms of the translation operators for the B sites. For a particular unit cell, the nearest neighbours of site A can be expressed in terms of the coordinates of site B in the same unit cell,

acted on by the translation operators $\gamma_{1,2,3,4}$ to get the relative translation operations \mathbb{I} , $\gamma_1\gamma_2^{-1}, \gamma_2\gamma_3^{-1}, \gamma_1\gamma_4\gamma_3^{-1}, \gamma_2\gamma_3^{-1}\gamma_4\gamma_3^{-1}$. Since we are concerned only with the $U(1)$ phases for a hyperbolic Bloch theory, we can use a linear change of basis for the \mathbf{k} -vector corresponding to the four-dimensional wave vector parametrising the Brillouin zone to get a simpler form for the Bloch phases. Using this transformation, the Bloch phases acquired due to the translation become $1, e^{ik_1}, e^{ik_2}, e^{ik_3}, e^{ik_4}$, respectively [8].

In terms of the Bloch phases, we can write a tight binding Hamiltonian in the sublattice basis as

$$\hat{H}_0 = \begin{pmatrix} V_{AA} & -t_{0a} - t_{1a}e^{ik_1} - t_{2a}e^{ik_2} - t_{3a}e^{ik_3} - t_{4a}e^{ik_4} \\ -t_{0b} - t_{1b}e^{-ik_1} - t_{2b}e^{-ik_2} - t_{3b}e^{-ik_3} - t_{4b}e^{-ik_4} & V_{BB} \end{pmatrix}, \quad (1)$$

where V_{AA} and V_{BB} are the on-site potentials at sublattice A and B, t_{ia} is the hopping from different B sites to the A site, and t_{ib} represents hopping from different A sites to the B site. We shall take the hermitian hoppings to be real and equal to unity. The usual flat space graphene can be obtained from this model by setting $k_3 = 0$ and $k_4 = \pi$. We note that tuning k_3 and k_4 provide additional degrees of freedom to the off diagonal term $h(\mathbf{k}) := 1 + e^{ik_1} + e^{ik_2} + e^{ik_3} + e^{ik_4}$. We will be treating the \mathbf{k} -vectors as parameters in order to study the positions of EPs and nodal points in cross-sections of the Brillouin zone for ease of representation. The simplicity of the Hamiltonian allows us to obtain analytical expressions for various quantities, which will be useful for analysing exceptional contours and other features upon introducing non-Hermiticity.

In the second quantized form, the Hamiltonian H can be written in terms of the creation and annihilation operators for the unit cell with the sublattice orbitals included through the Pauli matrices.

$$H = \sum_i V_0 c_i^\dagger \sigma_0 c_i + \sum_i M c_i^\dagger \sigma_z c_i + \sum_{\langle i,j \rangle} t c_i^\dagger \sigma_x c_j, \quad (2)$$

In terms of the k -space Hamiltonian \hat{H}_0 defined earlier, $V_0 = (V_{AA} + V_{BB})/2$, and $M = (V_{AA} - V_{BB})/2$ define the chemical potential and the sublattice potential, respectively. Since V_0 is simply a constant shift in the spectrum, we will set $V_0 = 0$, such that the sublattice potential ($\pm M$) is the only diagonal term. The hopping is restricted to be between nearest

neighbour unit cells.

In the sublattice basis, the time-reversal symmetry operator is just the complex conjugation operator $\mathcal{T} = \mathcal{K}$. The tight-binding Hamiltonian obeys time-reversal symmetry since $\mathcal{T}H\mathcal{T}^{-1} = H$. On the other hand, the particle-hole symmetry interchanges the sublattice basis, and the operator has the form $\mathcal{P} = \sigma_x\mathcal{K}$. $\mathcal{P}H\mathcal{P}^{-1} \neq -H$, and hence the Hermitian system only has time-reversal symmetry.

B. Introducing non-hermiticity

We will introduce non-hermiticity of various kinds through on-site gain and loss (terms proportional to σ_z), and non-reciprocal hopping (terms proportional to $\sigma_{x,y}$), using terms of the form $i\delta\sigma_z$, $i\Omega\sigma_y$, and $i\Gamma\sigma_x$. For simplicity, we will consider the non-Hermitian terms to be independent of k . All of these terms will break the time-reversal symmetry of the Hermitian model, with $\mathcal{T}H(\mathbf{k})\mathcal{T}^{-1} \neq H(-\mathbf{k})$. We will see how this anisotropy in the non-Hermiticity gives a richer complex energy spectrum with interesting windings of energy bands around EPs. Further, the high dimensionality of the k -space endows greater freedom in tuning the parameters of the system, allowing us to realise rich non-Hermitian phenomena. This freedom will have an even greater significance in obtaining higher-order EPs for tessellations with larger unit cells, such as the four band $\{8,4\}$ model, which will be discussed later.

IV. MODEL DIAGNOSTICS

A. Hermitian regime

We first briefly summarize the properties of the Hermitian model. In the Hermitian regime, the parameters at our disposal are the on-site potential $\pm M$ and the hopping strength t (assumed to be isotropic). The energy spectrum is similar to Euclidean graphene, with the additional freedom furnished by k_3 and k_4 providing additional tuning parameters on the k_1 - k_2 cross-section. Plotting cross-sections for the energy spectrum for different choices of k_3, k_4 can give nodal points as well as nodal lines as shown in Fig. 2(a)-(b). The nodal surface is visualised in Fig. 2(c), where those values of k_1, k_2, k_3 are plotted for which there exists a node for some value of k_4 . Fig. 2(f) shows the variation of the energy spectrum through different points in the four-dimensional Brillouin zone.

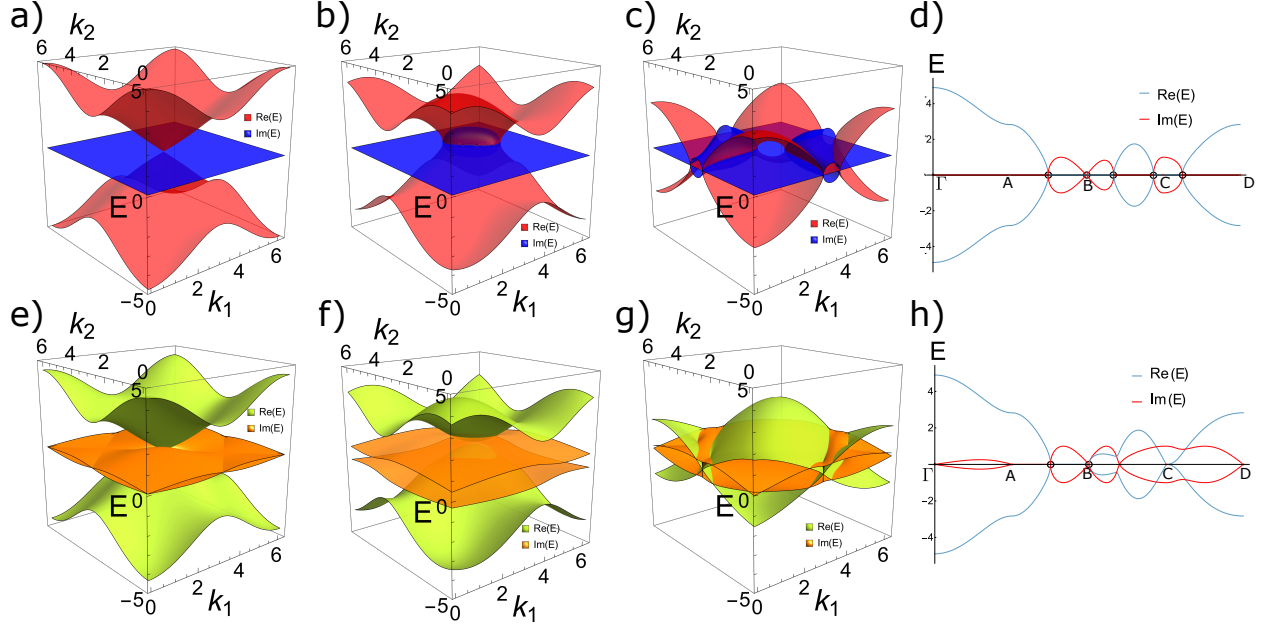


FIG. 3. **Energy spectra for the non-Hermitian cases with gain and loss (δ), and non-reciprocity (Γ).** (a)-(c) The shape of the nodal contour on the projected $k_1 - k_2$ plane with varying k_3 and k_4 for the case of gain and loss. (a) For $\delta = 1, k_3 = k_4 = 0$ gives the limiting case of a single band intersection point $\vec{k}_0 = (\pi, \pi, 0, 0)$. The dispersion near this point is quadratic in $\mathbf{k} - \mathbf{k}_0$. (b) A single nodal loop is obtained for $\delta = 1, k_3 = k_4 = \pi$. The spectrum scales as $E \sim (|\mathbf{k} - \mathbf{k}_0|)^{\frac{1}{2}}$ near the nodal contour. (c) Nodal contours obtained for $\delta = 1, k_3 = 7\pi/6, k_4 = \pi/4$ (d) The energy spectrum on the same path (but with $\delta = 1$) as in Fig. 2 (f). The points where both the energy levels become degenerate are marked with hollow circles, and occur when $|h(\mathbf{k})| = \delta$. (e)-(g) The energy bands and corresponding nodal contours for different choices of parameters (Γ, k_3, k_4) , i.e., non-reciprocal hopping case. (e) Similar to (a), one obtains a single nodal point where the bands touch. The choice of parameters is $\Gamma = 0.5, k_3 = \arccos(3/4), k_4 = 2\pi - k_3$. The dispersion is quadratic in k near the nodal point. (f) Absence of nodal points, with a finite complex gap in the spectrum for parameter values $\Gamma = 0.7, k_3 = k_4 = \pi/2$. (g) For $\Gamma = 0.5, k_3 = 4\pi/3, k_4 = 4\pi/5$, open nodal contours are obtained, where the spectrum scales as $E \sim (|\mathbf{k} - \mathbf{k}_0|)^{\frac{1}{2}}$, where k_0 is a point on the nodal contour. (h) The energy spectrum is shown on the above-mentioned path, with $\Gamma = 1$. There are two nodal points where both the real and imaginary parts of the eigenvalues become equal.

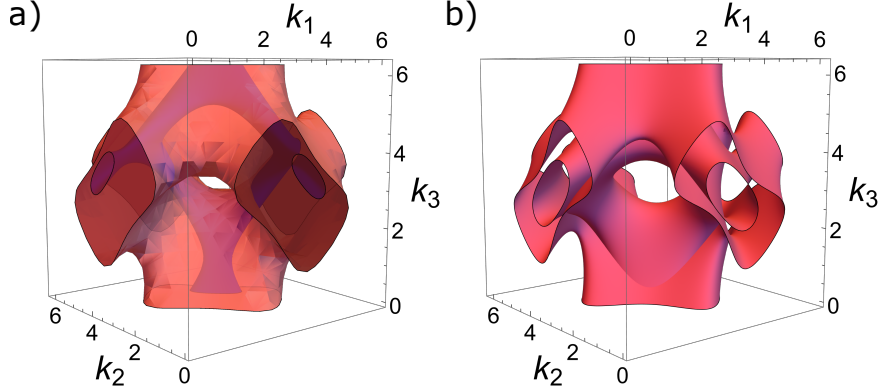


FIG. 4. **Exceptional nodal Surfaces for non-Hermitian hyperbolic graphene.** (a) The exceptional nodal surface values of k_1, k_2, k_3 for which there is a k_4 that results in a node in the four-dimensional Brillouin zone for $\delta = 0.5$ is shown in pink. The underlying blue region is the nodal contour for when $k_4 = \pi/2$. (b) The nodal contour for $\Gamma = 0.5$, where the contour becomes a two-dimensional surface compared to the three-dimensional volume in (a). This is due to the additional constraint placed by the $2i\Gamma\text{Im}(h)$ term in Eq. 9, thus reducing the degrees of freedom of the spectrum.

A sublattice potential M introduces a gap (equal to $2M$) in the system, and the linear dispersions at the Dirac points are replaced by quadratic dispersions at the band extrema, as shown in Fig. 2(d)-(e).

B. Non-Hermiticity and Phase Rigidity

We will introduce non-Hermiticity in two ways – through an imaginary on-site gain and loss and through non-reciprocal hopping within the unit cell. For the non-Hermitian Hamiltonian, the usual orthogonality of eigenvectors is replaced by the weaker condition of *biorthogonality* [36]. This gives us the eigenvectors for H (right eigenkets $|R_i\rangle$) and H^\dagger (left eigenkets $|L_i\rangle$) obeying the biorthogonality condition

$$\langle L_i | R_j \rangle = \delta_{ij}, \quad (3)$$

where δ_{ij} is the Kronecker delta function. Recall that at EPs, two or more eigenvectors coalesce and hence the above relation falls through since if $|R_i\rangle = |R_j\rangle$ then their inner products with $\langle L_i|$ (expected to be 1 and 0 respectively) must also be equal, contrary to the

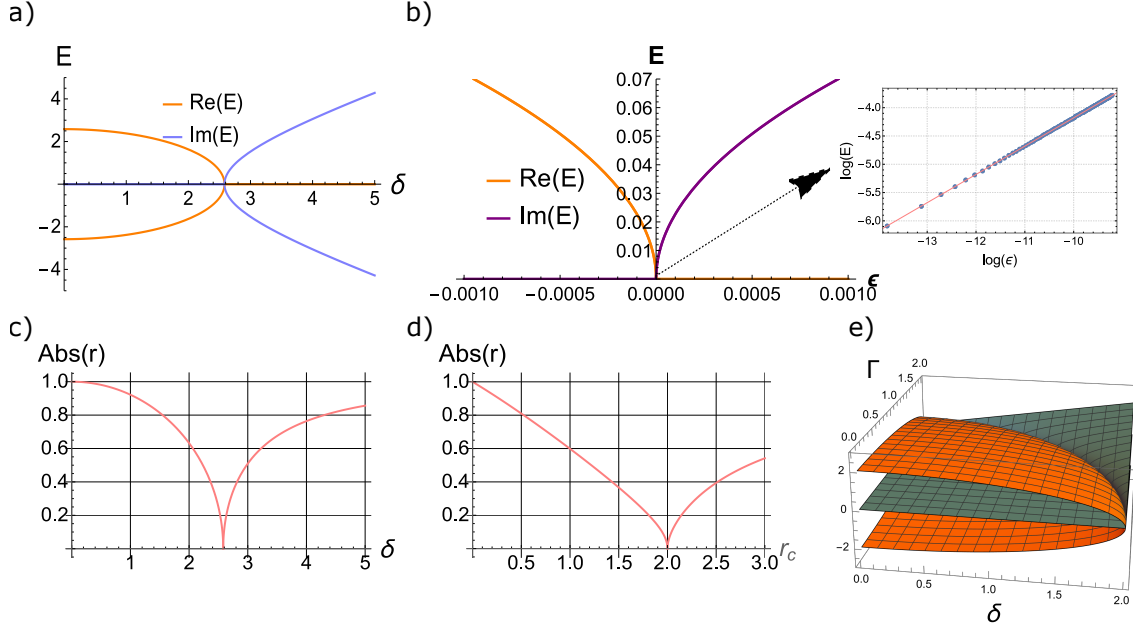


FIG. 5. **Diagnosing exceptional points using phase rigidity.** (a) The energy spectrum as a function of δ for $\mathbf{k} = (\pi/2, \pi/3, 3\pi/4, \pi)$. The bands touch each other when $\delta = |h(\mathbf{k})| \approx 2.58145$. (b) The scaling of the energy very close to the EP ($\delta = |h(\mathbf{k})| + \epsilon$, where ϵ is a perturbation from the EP). The inset shows the logarithmic scale plot, which has a slope of 0.5, revealing a square root dependence on ϵ characteristic of second-order EPs. (c) The magnitude of the phase rigidity, r , as a function of δ for the same \mathbf{k} . (d) For a system with both non-reciprocity (Γ) and on-site gain and loss (δ) parametrised by $\delta = r_c \cos \theta$, $\Gamma = r_c \sin \theta$, the spectrum is independent of θ . For $k_1 = 4\pi/3, k_2 = 0, k_3 = 2\pi/3, k_4 = 0$, the condition for obtaining a gapless point is $r_c = 2$. The phase rigidity is shown to go to zero as a function of r_c , with $\theta = \pi/4$. (e) The circular exceptional contour in the $\delta - \Gamma$ parameter space for $\mathbf{k} = (0, 0, 2\pi/3, 4\pi/3)$.

statement of the condition. We will use this as a measure of the proximity to an EP using the phase rigidity, r , which measures the extent of mixing of the wave functions around an EP through the deviation of the normalisation from unity [37]. The phase rigidity for a band is defined as

$$r_j = \frac{\langle L_j | R_j \rangle}{\langle R_j | R_j \rangle}. \quad (4)$$

This phase rigidity provides a quantitative measure of the biorthogonality. Furthermore, the vanishing of the phase rigidity near an EP allows defining an exponent around the

EPs. For instance, the scaling exponents around an N -th order EP can be $(N - 1)/N$ or $(N - 1)/2$ [38]. Remarkably, phase rigidity is not just a theoretically defined quantity, but has also been experimentally measured [39]. We will use phase rigidity to diagnose the EPs in our hyperbolic lattice models.

1. On-Site Gain and Loss

First, we add an on-site gain and loss of strength δ , which amounts to adding $i\delta\sigma_z$ to the Bloch Hamiltonian. As a result, the spectrum is no longer entirely real. In fact, the eigenvalues $\lambda = \pm\sqrt{|h|^2 - \delta^2}$ will be purely real or purely imaginary.

For a non-zero M , the square root has a constant non-zero imaginary part which prohibits any band touchings, even in the individual real and imaginary spectra. The locus of the real and imaginary energies (E_r and E_i) is the intersection of three hyperbolic surfaces, given by,

$$E_r E_i = M\delta, \tag{5}$$

$$E_r^2 - E_i^2 \leq M^2 + 25 - \delta^2, \tag{6}$$

$$E_r^2 - E_i^2 \geq M^2 - \delta^2. \tag{7}$$

Evidently, increasing the non-Hermiticity strength δ will lead to a more prominent imaginary spectrum. For $M = 0$, we find that either the real or the imaginary part of the eigenvalues will vanish, and we can recover nodal contours where the eigenvalues are zero, with the cross-sections shown in Fig. 3(a)-(d) for some choices of k_3, k_4 . The nodal contours mark the transition from purely real to purely imaginary eigenvalues. In Fig. 3(d), a one-dimensional contour is parametrised in the Brillouin zone, which shows the appearance of EPs marked in black. Contours connecting these EPs are characterised by purely real or purely imaginary energy eigenvalues, and are called non-Hermitian Fermi arcs [18]. While these arcs occur trivially due to the behaviour of the band structure for this case, we will observe their existence even for non-reciprocal hopping in the next section. In the limit $\delta > 5t$, the spectrum becomes purely imaginary, and the bands do not touch in the four-dimensional Brillouin zone.

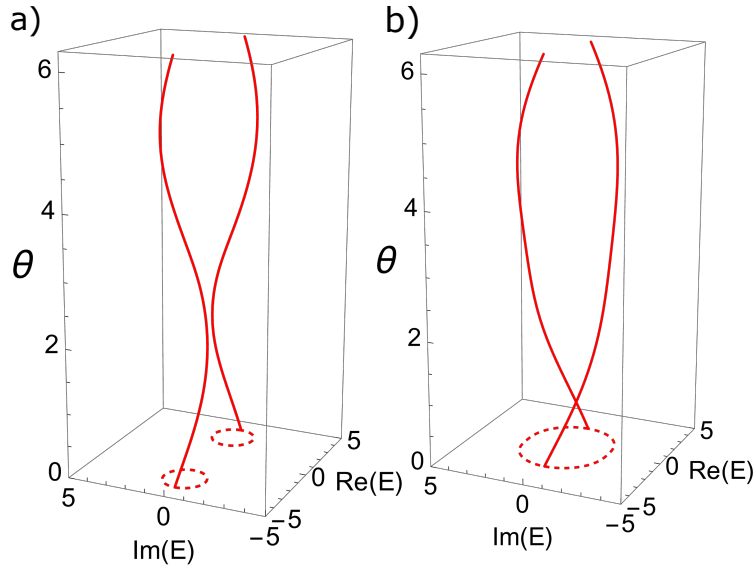


FIG. 6. **Inter-Band winding for the $\{10,5\}$ tessellation.** (a) Illustration of the winding of energy levels for the $\{10,5\}$ tessellation with the on-site gain and loss. For the parameter choice $k_1 = 2\pi/3, k_2 = \pi/3, k_3 = 0, k_4 = 0$ and $\delta = 2$, the Hamiltonian is not defective, and we get trivial winding of the energy levels with respect to a parametric perturbation $e^{i\theta}\sigma_x$. (b) $\delta = 2\sqrt{3}$ makes the Hamiltonian rank-deficit and gives an EP at the chosen \vec{k} -point. In this case, we can see the inter-band winding visualised through the exchange of the energy levels in one complete cycle of the perturbation.

2. Non-Reciprocal Hopping

Another way to introduce non-Hermiticity is through non-reciprocal hopping within the unit cell. This can be done by adding terms of the form $i\Gamma\sigma_x$ or $i\Omega\sigma_y$. These terms produce an imaginary k -dependent term in the expression for the eigenvalues, given by

$$i\Omega\sigma_x : E_{\pm} = \pm\sqrt{|h|^2 + M^2 - \Omega^2 + 2i\Omega\text{Re}(h)}, \quad (8)$$

$$i\Gamma\sigma_y : E_{\pm} = \pm\sqrt{|h|^2 + M^2 - \Gamma^2 - 2i\Gamma\text{Im}(h)}. \quad (9)$$

To obtain a node, both the real and imaginary parts in the square root must go to zero. This adds additional structure to the nodes which is sensitive to the presence of the non-Hermitian term. The shape of the nodal surface drastically changes upon the addition of a

very small non-reciprocity and cannot be treated as a perturbation on the original surface, as shown in Fig. 4. Typical two-dimensional cross-sections of the eigenspectra are shown in Fig. 3(e)-(h), with different characters for the nodal regions, which could be a nodal point (e), a nodeless cross-section (f), or a nodal contour (g). Fig. 3(h) shows the variation of the spectrum on a one-dimensional contour in the Brillouin zone. The appearance of the nodal EPs is shown in black, where both the real and imaginary parts of the eigenvalues are equal. These nodes are connected through non-Hermitian Fermi arcs where the real part of the energy goes to zero, as shown by our choice of contour. For the case of the $i\Gamma\sigma_y$, the condition for the appearance of nodes is obtained to be

$$|h|^2 = \Gamma^2 - M^2,$$

$$\Gamma\text{Im}(h) = 0.$$

Therefore, for non-zero Γ , we require $h = \pm\sqrt{\Gamma^2 - M^2}$. The requirement for the imaginary part to be zero results in lower dimensional nodal surfaces on the k_1, k_2 cross-section as shown in Fig. 4(b). Similarly, the nodal spectrum for non-reciprocity $i\Omega\sigma_x$ is obtained by setting $h = \pm i\sqrt{\Omega^2 + M^2}$.

C. Identifying Exceptional Points

At the EPs, the coalescing of the eigenvalues and eigenvectors causes the Hamiltonian to become defective due to the absence of a complete basis to span the Hilbert space [18]. EPs lead to degeneracies in the spectrum, which in our case can only occur if the eigenvalues are zero (since the spectrum is symmetric about $E = 0$). Thus, the nodal surfaces that we obtained earlier correspond to the intersections of the Fermi arcs for the real and imaginary parts of the energy leading to second-order EPs. We will subsequently investigate the occurrence of higher-order EPs in a four-band model for the $\{8,4\}$ tessellation.

The phase rigidity, r , for an eigenvector measures the proximity to an EP. In the Hermitian limit, the left and right eigenkets are equal, and hence $r = 1$. As the non-Hermiticity is increased, the left and right eigenkets become unequal and their inner product starts to decrease as the eigenkets start to mix. At the EPs, the left and right eigenkets are orthogonal and $r = 0$. Therefore, analyzing the phase rigidity on momentum-space cross

sections indicates the proximity from an EP. For second-order EPs, the eigenspectrum shows a square-root scaling, which is indicated in Fig. 5(a)-(b). The complex eigenspectrum of the non-Hermitian system allows the definition of the winding of energy eigenvalues as a topological invariant [18]. One can define an analogous winding of the relative phase for the eigenvalues on a contour, \mathcal{C} , encircling an EP, which will be quantised and indicates a coalescence of the eigenvectors. This vorticity ν_{nm} for energy bands E_n and E_m can be defined as

$$\nu_{nm} = \frac{1}{2\pi} \oint_{\mathcal{C}} \nabla_{\mathbf{k}} \arg(E_n(\mathbf{k}) - E_m(\mathbf{k})) \cdot d\mathbf{k}, \quad (10)$$

For a contour \mathcal{C} encircling the EP, $\nu_{nm} = \pm 1/2$ for the second order EP in our model. This is shown in terms of a parametrisation of a circular path centred at the EP in Fig. 6, and leads to an exchange of the eigenvalue and eigenvectors across the EP.

D. Higher order Exceptional Points in $\{8,4\}$ Tessellations

In recent years, higher-order EPs – where more than two eigenvalues and eigenvectors merge – have been of significant interest owing to their remarkable properties beyond second-order EPs. Here, we next show how hyperbolic lattice models allow such higher-order EPs in the presence of non-Hermiticity. As an example, we consider the $\{8,4\}$ tessellation, which is part of the $\{4g, 4\}$ infinite family of tessellations with genus 2 [34]. The unit cell has four sites and the Bolza lattice is an $\{8,8\}$ tessellation, with the Fuchsian group generated by four elements. We introduce the tight-binding Hamiltonian with balanced complex gain and loss, $\pm i\delta$, on two sites

$$H_0(\mathbf{k}) = \begin{pmatrix} i\delta & 1 + e^{i(k_1 - k_2)} & 0 & e^{ik_1} + e^{-ik_4} \\ 1 + e^{i(k_2 - k_1)} & 0 & 1 + e^{i(k_2 - k_3)} & 0 \\ 0 & 1 + e^{i(k_3 - k_2)} & 0 & 1 + e^{i(k_3 - k_4)} \\ e^{-ik_1} + e^{ik_4} & 0 & 1 + e^{i(k_4 - k_3)} & -i\delta \end{pmatrix}. \quad (11)$$

To study the EPs generated in this model, we use the Newton polygon method elaborated in Ref. 38. We begin by introducing a perturbation, ϵ , to the hopping from site A and B such that the perturbed Hamiltonian becomes

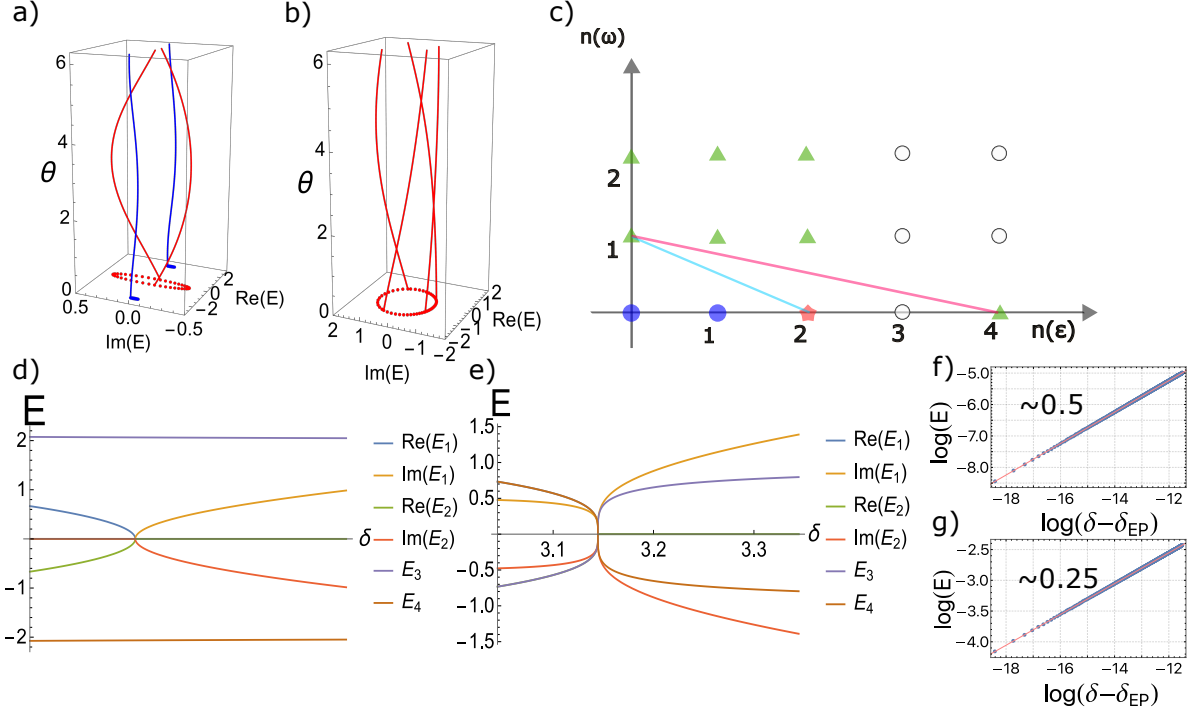


FIG. 7. **Inter-band winding and higher-order EPs in $\{8,4\}$ tessellation.** (a) The eigenvalue winding for the second order EP. The bands in red show an exchange whereas the bands in blue return to their original values under a cyclic perturbation with $\epsilon = 0.07e^{i\theta}$. This gives a second-order EP. The parameters taken here are $k_1 = \pi/4, k_2 = 2\pi/3, k_3 = 3\pi/5, k_4 = 61\pi/60$ and $\delta \approx 2.07923$. (b) The fourth order EP, where $k_1 = k_2 = 0, k_3 = k_4 = \arccos(2\sqrt{5} - 5)$ and $\delta \approx 3.14461$. Panel (c) shows the Newton polygon diagram for the $\{8,4\}$ model considered above. The hollow circles show the terms that are absent in the characteristic polynomial. The blue circles are the terms that need to vanish to obtain a second-order EP, whose bounding line is shown in blue. The red point is the additional term that needs to vanish to reach a fourth-order EP, whose bounding line is shown in red. Panels (d) and (e) show the energy spectrum near the EP for the second and fourth-order EPs, respectively. The scaling for the spectra is shown in (f) and (g), respectively. The lowest-order perturbation terms in the spectra have scaling coefficients 0.5 and 0.25, respectively.

$$H(\mathbf{k}) = \begin{pmatrix} i\delta & 1 + e^{i(k_1-k_2)} + \epsilon & 0 & e^{ik_1} + e^{-ik_4} \\ 1 + e^{i(k_2-k_1)} + \epsilon & 0 & 1 + e^{i(k_2-k_3)} & 0 \\ 0 & 1 + e^{i(k_3-k_2)} & 0 & 1 + e^{i(k_3-k_4)} \\ e^{-ik_1} + e^{ik_4} & 0 & 1 + e^{i(k_4-k_3)} & -i\delta \end{pmatrix}. \quad (12)$$

Briefly, we use a Puiseux series based approach to characterise the leading order expansion of a Hamiltonian in the vicinity of an EP. Using the leading order term in the expansion, we can find the order of an EP using the characteristic $1/N$ scaling for an N -th order EP. For a non-trivial contour parametrised by some ϵ , the characteristic polynomial $P(\omega) = \det(H - \omega\mathbb{I}) = \sum_{m,n} h_{mn}\omega^m\epsilon^n$ for the Hamiltonian with a perturbation of strength ϵ can be written as a binomial in terms of ω and ϵ . Plotting the powers (m, n) for the coefficients $h_{mn}\omega^m\epsilon^n$ in the binomial gives us the order of the EP using the slope of the segment with all the points on or to the right of it.

The Newton polygon diagram for our Hamiltonian is shown in Fig. 7 (c). Using the analytic form for the characteristic polynomial, we can make different parameter choices to eliminate the (0,0) and (1,0) points on the diagram to obtain a second-order EP in the system. Subsequently, we can also remove the (2,0) point to obtain a fourth-order EP. The energy spectra for the four bands are shown in Fig. 7(d)-(e) for the second and fourth-order EPs, respectively. The E_3, E_4 bands in Fig. 7(d) do not mix and remain purely real. The scaling for E_1, E_2 bands is shown in Fig. 7(f), revealing a square root dependence on the parameters.

Similarly, for the fourth-order EP, all four bands participate in the mixing process and scale more steeply as a function of δ . The logarithmic scaling shows a $\delta^{1/4}$ dependence on the parameters, as expected. The expected scaling is shown for the spectrum near the EPs in both cases in Fig. 7(f) and (g), thereby confirming the higher order EPs in this model.

V. IMPLICATIONS IN REAL SPACE: POINCARÉ DISK

Till now, we have focused on the reciprocal space picture of the exceptional contours. Next, we construct a real space system for the $\{10,5\}$ tessellation using the process of circular inversion as outlined in Ref. 11. This procedure allows the construction of successive epochs of the hyperbolic lattice recursively. The number of sites in each successive epoch increases

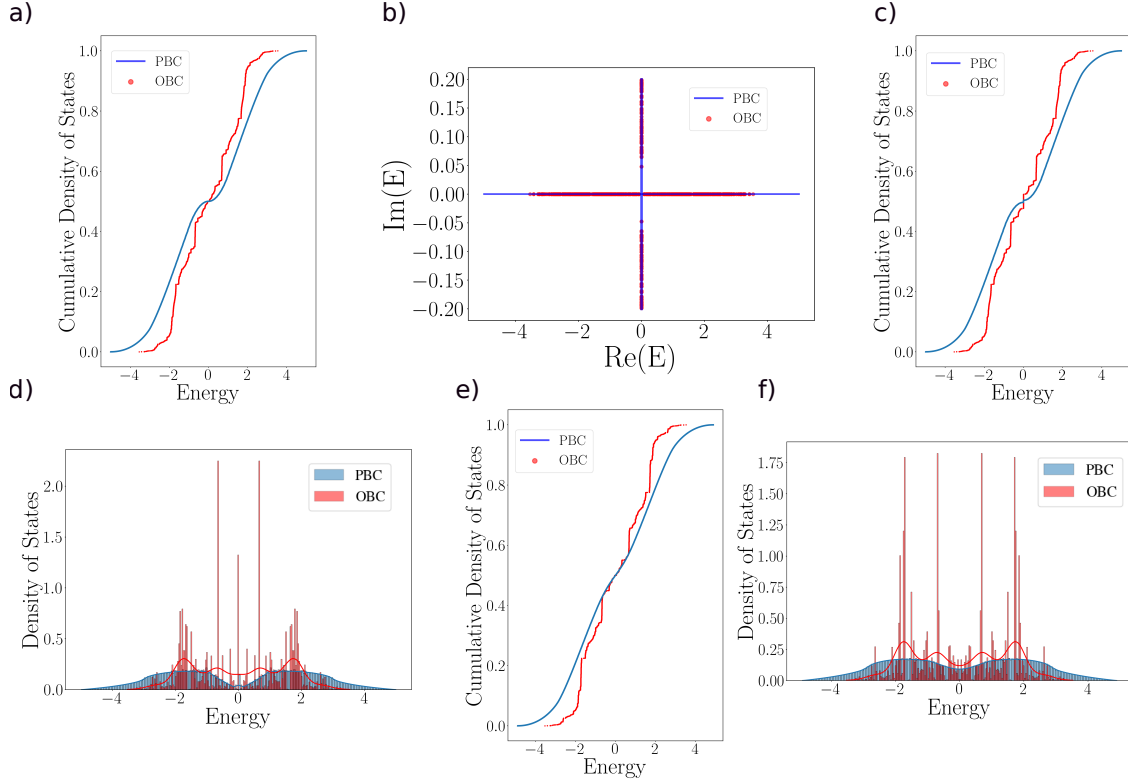


FIG. 8. **Energy spectra and densities of states.** (a) The density of states in a cumulative probability distribution for the k -space model with periodic boundaries and the open boundary system. (b) The complex energy spectra with on-site gain and loss ($\delta = 0.2$). The open boundary spectrum is a subset of the periodic boundary condition spectrum. (c) The cumulative density of states for the system with $\delta = 0.2$. The density is measured with respect to only the real part of the energy, leading to a spike in the probability distribution at $E = 0$ corresponding to the spectrum along the imaginary axis. (d) A kernel density estimate for the density of states with $\delta = 0.2$. The corresponding histogram for the finite distributions is smoothed to give the darker outlines. (e) The cumulative density of states for the system with non-reciprocity $\Omega = 0.2$, with the corresponding density of states profile shown in (f).

exponentially, and we limit the system size to four epochs (which amounts to 7040 lattice sites in real space).

Defining the sublattice and unit cells is a recursive variation of the dimer covering problem on the hyperbolic lattice and results in a few dangling sites at the boundary which are not paired into any unit cell. This manifests itself as a perturbation that breaks the tenfold rotational symmetry of the lattice.

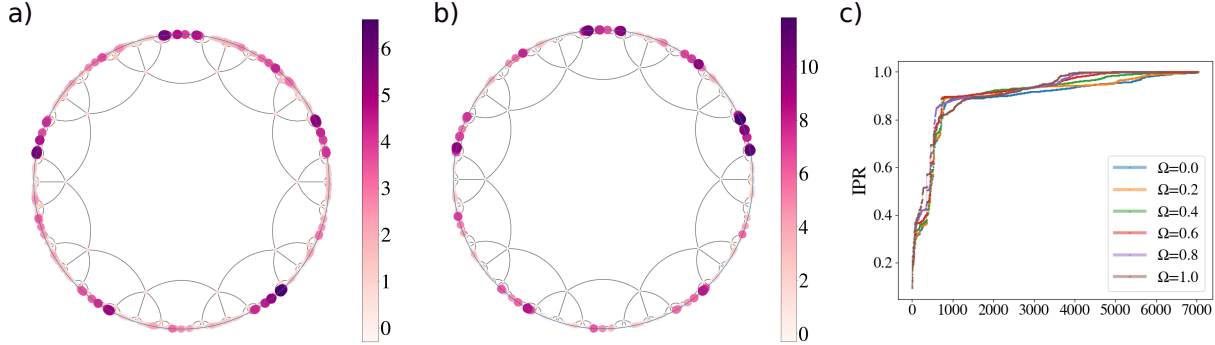


FIG. 9. **Localisation effects with non-reciprocal hopping.** The density of states summed over all the eigenfunctions for the system with two different values of the non-reciprocity parameter (a) $\Omega = 0.2$ and (b) $\Omega = 0.4$. Although localisation can be seen at the outer epochs, the profile is not tenfold rotationally symmetric due to the asymmetry while defining unit cells for non-Hermitian hopping. The extent and magnitude of boundary localisation increase with Ω . The asymmetry in the localisation is more evident for larger values of Ω . (c) The inverse participation ratio (IPR) for eigenvectors with different values of non-reciprocity. The macroscopic fraction of boundary sites leads to a high IPR even for states of the Hermitian system. The absence of an extensive shift of boundary localised modes with non-reciprocity rules out the possibility of a skin effect in this class of models.

We numerically compute the density of states with respect to the real part of the energy. Fig. 8(a) shows the comparison of the density of states obtained for the Hermitian system under open boundaries and in the k -space. The deviation between the two is due to the macroscopic fraction of boundary sites for hyperbolic tessellations. We note that recently the process of using regular maps to obtain a boundary-removed periodic spectrum has been proposed [8, 15] to get better agreements with the k -space density of states. However, we will use open boundary spectra to probe localisation effects in the non-Hermitian hyperbolic system. Remarkably, boundary removed spectra for $\{p, q\}$ tessellations with higher ' q ', including the $\{10, 5\}$, have been shown to display considerable deviation from the band theoretic predictions [8].

The spectra and density of states for the system with gain and loss are shown in Fig. 8(b)-(d). The open boundary spectrum is a subset of the periodic boundary condition spectrum as seen in Fig. 8(b) – this is consistent with the theorem outlined in Ref. 40. Whereas the local density of states profile does not show any localisation features, the density of states

shows a jump at zero energy due to a large number of states with purely imaginary energy.

Upon adding non-reciprocal hopping, we notice a localisation at the outer epoch of the system, as shown in Fig. 9(a)-(b). The localisation increases with non-reciprocity and has an asymmetric profile due to the method of defining the unit cells, as discussed above. We use the inverse participation ratio (IPR) to study this localisation by measuring the fraction of wave-function probability at the boundary. The IPR for an eigenket $|\psi_n\rangle$, is defined as

$$IPR = \frac{\sum_{r \in \text{boundary}} |\langle \mathbf{r} | \psi_n \rangle|^2}{\sum_r |\langle \mathbf{r} | \psi_n \rangle|^2}. \quad (13)$$

The numerator calculates the total occupation probability of boundary sites, normalised by the total probability density. Plotting the IPR for different values of non-reciprocity in Fig. 9(c) reveals that the non-reciprocity does not cause a skin effect in the Hamiltonian and is simply a perturbation to the density profile, enhanced by the microscopic probability density in the wave-function density profile. In the Hermitian limit under the Bloch ansatz itself, having a macroscopic number of sites at the boundary leads to states with a large IPR, as can be seen from the plot with $\Omega = 0.0$ in Fig. 9(c). So, we can rule out the possibility of a skin effect in this class of models, which is also consistent with the absence of a point gap in the periodic boundary condition energy spectrum.

VI. SUMMARY AND OUTLOOK

In summary, we have proposed introducing non-Hermiticity in hyperbolic lattices to obtain a rich platform for exploring exceptional degeneracies. By means of a range of analytical and numerical tools, we demonstrated highly tunable exceptional points and contours in $\{10,5\}$ tessellations in the presence of on-site gain and loss and non-reciprocal hopping. We used phase rigidity, energy scaling and vorticity to diagnose these exceptional structures. Further, using the $\{8,4\}$ tessellation lattice as an example, we showed the appearance of higher-order exceptional contours by means of the recently proposed Newton polygon approach. We further examined the open boundary spectra in the Poincaré disk and showed the localisation at the boundaries. Given the recent experimental realization of both hyperbolic lattices [7, 8] and non-Hermitian phases [25–27] in a plethora of platforms, we are hopeful that our predictions of exceptional degeneracies can be readily realized in state-of-the-art experimental setups. We hope our work motivates further theoretical and experimental

explorations of non-Hermitian hyperbolic matter.

Note Added: During the final stages of this work, we came across a complementary preprint, which studies the skin effect in hyperbolic topological lattice models [41].

ACKNOWLEDGMENTS

We thank Adhip Agarwala and Vijay Shenoy for illuminating discussions. N.C. acknowledges a fellowship from the Kishore Vaigyanik Protsahan Yojana (KVPY). A.N. is supported by the Indian Institute of Science.

-
- [1] A. Friedmann, in *A Source Book in Astronomy and Astrophysics, 1900–1975* (Harvard University Press, 1979) pp. 838–843.
 - [2] R. Brooks, in *Proc. Ashkelon Workshop on Complex Function Theory* (Citeseer, 1996) pp. 61–73.
 - [3] C. Monthus and C. Texier, *Journal of Physics A: Mathematical and General* **29**, 2399 (1996).
 - [4] D. Krioukov, F. Papadopoulos, M. Kitsak, A. Vahdat, and M. Boguná, *Physical Review E* **82**, 036106 (2010).
 - [5] N. P. Breuckmann, C. Vuillot, E. Campbell, A. Krishna, and B. M. Terhal, *Quantum Science and Technology* **2**, 035007 (2017).
 - [6] S. Mertens and C. Moore, *Physical Review E* **96**, 042116 (2017).
 - [7] A. J. Kollár, M. Fitzpatrick, and A. A. Houck, *Nature* **571**, 45 (2019).
 - [8] A. Chen, H. Brand, T. Helbig, T. Hofmann, S. Imhof, A. Fritzsche, T. Kießling, A. Stegmaier, L. K. Upreti, T. Neupert, *et al.*, *Nature Communications* **14**, 622 (2023).
 - [9] J. Maciejko and S. Rayan, *Science advances* **7**, eabe9170 (2021).
 - [10] D. M. Urwyler, P. M. Lenggenhager, I. Boettcher, R. Thomale, T. Neupert, and T. Bzdušek, *Physical Review Letters* **129**, 246402 (2022).
 - [11] Z.-R. Liu, C.-B. Hua, T. Peng, and B. Zhou, *Physical Review B* **105**, 245301 (2022).
 - [12] Z.-R. Liu, C.-B. Hua, T. Peng, R. Chen, and B. Zhou, *Physical Review B* **107**, 125302 (2023).
 - [13] Y.-L. Tao and Y. Xu, *Physical Review B* **107**, 184201 (2023).

- [14] J. Maciejko and S. Rayan, Proceedings of the National Academy of Sciences **119**, e2116869119 (2022).
- [15] A. Stegmaier, L. K. Upreti, R. Thomale, and I. Boettcher, Physical Review Letters **128**, 166402 (2022).
- [16] Y. Ashida, Z. Gong, and M. Ueda, Advances in Physics **69**, 249 (2020).
- [17] R. El-Ganainy, K. G. Makris, M. Khajavikhan, Z. H. Musslimani, S. Rotter, and D. N. Christodoulides, Nature Physics **14**, 11 (2018).
- [18] E. J. Bergholtz, J. C. Budich, and F. K. Kunst, Reviews of Modern Physics **93**, 015005 (2021).
- [19] A. Ghatak and T. Das, Journal of Physics: Condensed Matter **31**, 263001 (2019).
- [20] A. Banerjee, R. Sarkar, S. Dey, and A. Narayan, Journal of Physics: Condensed Matter (2023).
- [21] C. M. Bender, Reports on Progress in Physics **70**, 947 (2007).
- [22] W. Heiss, Journal of Physics A: Mathematical and Theoretical **45**, 444016 (2012).
- [23] M.-A. Miri and A. Alù, Science **363**, eaar7709 (2019).
- [24] Ş. K. Özdemir, S. Rotter, F. Nori, and L. Yang, Nature materials **18**, 783 (2019).
- [25] H. Hodaei, A. U. Hassan, S. Wittek, H. Garcia-Gracia, R. El-Ganainy, D. N. Christodoulides, and M. Khajavikhan, Nature **548**, 187 (2017).
- [26] W. Chen, Ş. Kaya Özdemir, G. Zhao, J. Wiersig, and L. Yang, Nature **548**, 192 (2017).
- [27] J. Wiersig, Photonics Research **8**, 1457 (2020).
- [28] S. Yao and Z. Wang, Physical review letters **121**, 086803 (2018).
- [29] V. M. Alvarez, J. B. Vargas, and L. F. Torres, Physical Review B **97**, 121401 (2018).
- [30] K. Yokomizo and S. Murakami, Physical review letters **123**, 066404 (2019).
- [31] D. S. Borgnia, A. J. Kruchkov, and R.-J. Slager, Physical review letters **124**, 056802 (2020).
- [32] X. Zhang, T. Zhang, M.-H. Lu, and Y.-F. Chen, Advances in Physics: X **7**, 2109431 (2022).
- [33] R. Lin, T. Tai, L. Li, and C. H. Lee, arXiv preprint arXiv:2302.03057 (2023).
- [34] I. Boettcher, A. V. Gorshkov, A. J. Kollár, J. Maciejko, S. Rayan, and R. Thomale, Physical Review B **105**, 125118 (2022).
- [35] R. Yuncken, arXiv preprint arXiv:1103.2051 (2011).
- [36] D. C. Brody, Journal of Physics A: Mathematical and Theoretical **47**, 035305 (2013).
- [37] H. Eleuch and I. Rotter, Physical Review A **93**, 042116 (2016).

- [38] R. Jaiswal, A. Banerjee, and A. Narayan, *New Journal of Physics* **25**, 033014 (2023).
- [39] W. Tang, X. Jiang, K. Ding, Y.-X. Xiao, Z.-Q. Zhang, C. T. Chan, and G. Ma, *Science* **370**, 1077 (2020).
- [40] N. Okuma, K. Kawabata, K. Shiozaki, and M. Sato, *Physical review letters* **124**, 086801 (2020).
- [41] J. Sun, C.-A. Li, S. Feng, and H. Guo, *arXiv preprint arXiv:2305.19810* (2023).